Department of Applied Physics *(Coherence and Quantum Technology)*
Advanced Research Center for Nanolithography *(Plasma Theory and Modelling)*

Recombination in an expanding laser-produced tin plasma for EUV lithography

External Internship (15 EC)

S. Schouwenaars
1000983

CQT 2022-20

TU/e Supervisor:
prof. dr. ir. O.J. Luiten

ARCNL Supervisor:
dr. John Sheil

Amsterdam, January 2023

Abstract

Modern-day lithography machines make use of an extreme ultraviolette (EUV)-emitting laser-produced plasma (LPP) generated from tin microdroplets. As this plasma expands, mitigation of the ionic debris becomes key in preserving the lifetime of the EUV optics. Extensive characterization of the plasma expansion can aid in the design of effective mitigation schemes. Here, we present results of a theoretical study on the role of recombination in expanding tin LPPs relevant to EUV lithography. Knowledge on the rate of various recombination mechanisms is essential in determining the ionization balance some distance away from the target. A time-dependent collisional-radiative model is employed to study how three distinct recombination mechanisms (three-body, dielectronic and radiative) affect charge state populations. By using comprehensive atomic calculations of Badnell *et. al.* on the dielectronic rate coefficients, we demonstrate the importance of the dielectronic mechanism in expansion for the first time. Moreover, we compute estimates for the time (and distance) it takes for the charge states to freeze out for a range of initial electron temperatures and densities. This can be coupled to radiation-hydrodynamic codes such as RALEF-2D to quantify where the assumption of local thermal equilibrium (LTE) ionization breaks down. The code serves as a flexible numerical tool to study the effects of recombination.

Contents

1 Introduction

Light has become an indispensable tool to probe and manipulate matter at ever smaller scales. Examples include high-resolution biomedical imaging [1, 2], materials processing [3, 4] and a myriad of industrial applications [5]. Among these applications is also the continuation of Moore's law, that is the exponential increase in density of electronic components on a chip [6]. This endeavour heavily relies on the continued development of suitable light sources because, currently, optical lithography is a key step in the fabrication of nanoscale integrated circuits on chips [7]. In this photochemical process, light is used to image patterns on photosensitive coated surfaces of silicon substrates. Subsequently, a series of deposition, etching and development steps form these specific structures on microchips. Analogous to any other optical system, employing shorter wavelengths of light increases the spatial resolution at which the structures on chips can be manufactured. On a quest to reduce the size of chip features ever further, the wavelength requirements have since been pushed from the visible part of the spectrum deep into the extreme ultraviolet (EUV) regime of several nanometers [8]. As a consequence, the realization of a reliable and economical EUV light source is currently one of the most important engineering tasks in the realm of lithography.

1.1 Laser-produced tin plasma as EUV source

Nowadays, the technology of choice in state-of-the-art lithography machines is an EUV-emitting laser-produced plasma (LPP) generated from tin microdroplets [9]. Incorporating this particular technique in modern-day chip machines is primarily motivated by its power scalability and the ability to provide high fluxes of EUV at high repetition rates, which is desired for high-volume manufacturing [9, 10]. The manner in which an EUV-emitting LPP is generated from liquid tin droplets is schematically depicted in Fig. 1.1.

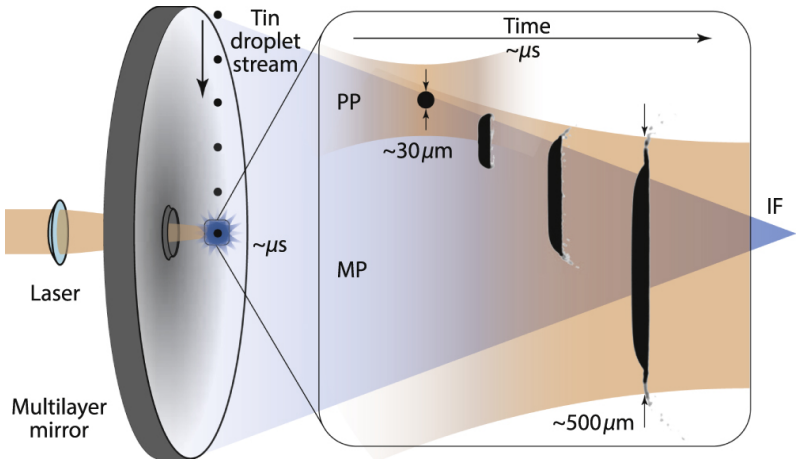

Figure 1.1: Schematic of the two-step process going from liquid tin droplets to an EUV-emitting LPP, taken from Ref. [11].

A stream of liquid tin droplets ($\sim$30 μm diameter across) is released from the nozzle of a droplet generator in a vacuum chamber at a 50 kHz rate, the droplets being subsequently irradiated by two laser pulses. First, a low-energy pre-pulse (PP) deforms the spherical droplets into pancake-like disks shapes, which are better suited to interact with the second pulse [12, 13]. The reason for this is for the target geometry (specifically its lateral size) to better couple to the incoming second laser pulse for optimum EUV generation [14]. This second pulse is a high-power main pulse (MP), which hits the deformed tin droplets and produces an extremely hot ($30 - 50$ eV), dense ($10^{19} - 10^{21}$ cm^{-3}) and highly ionized tin plasma which emits EUV radiation. In industrial settings, high-power CO_2–lasers operating at a laser wavelength of 10.6 μm are currently the standard for the MP, but solid-state Nd:YAG lasers at 1 μm may offer considerable advantages in the future, such as improved energy efficiency and better temporal pulse-shaping capabilities [15]. In addition, investigations into solid-state lasers operating at 2 μm have demonstrated capabilities for operation at higher rep rates and improved electrical efficiency compared to the CO_2 gas lasers [16].

The spectra recorded from these plasmas reveal an intense, narrow-band peak around a wavelength of 13.5 nm [17]. Crucially, this emission feature matches well with the 2% reflective bandwidth (referred to as the in-band radiation) of the multilayer mirrors (MLMs) based on molybdenum/-silicon (Mo/Si) [18]. This strong overlap in emission and reflection has established tin LPPs as the light source of choice for EUV lithography [19], as the generated EUV can be collected and guided away from the source vessel to the wafer stage by these MLMs. The strongly correlated electronic structure of the highly charged open-shell ions Sn^{+8}–Sn^{+13} is responsible for the strong emission of EUV light. In a paper by Torretti *et. al.* [20], it was found that the EUV light originates primarily from transitions between multiply-excited states, rather than singly-excited states which decay to the ground state. In addition, the transitions between these multiply-excited states occur in the same narrow-band window around 13.5 nm as the singly-excited states, and this holds true for a particularly wide range of charge states. These electronic properties of the tin ions can explain why specifically tin is an excellent emitter of the in-band radiation.

1.2 Ion debris mitigation

The efficiency of this type of EUV source is typically established on the basis of two characteristics [8, 21]. First, the conversion efficiency (CE), defined as the ratio between the in-band EUV light falling on the collector mirror and the input laser energy, must be high. Secondly, the plasma used to generate the light should not create large amounts of debris flying off in the form of highly energetic particles or liquid droplets. Steps have to be taken on both fronts to improve on current EUV sources. In this report, we will on the latter, specifically by characterizing the ionic debris.

After formation, the hot and dense tin plasma expands supersonically into its surroundings, which could potentially inhibit the EUV source performance in several ways. Among the main culprits are the highly energetic ions which could impinge upon the costly EUV optics through a combination of sputtering and ion implantation. For example, the EUV radiation emitted by the plasma is collected and focused by a large and expensive X-ray optic surrounding the plasma, as can be seen in Fig. 1.1. It is key for the optics to preserve their lifetime as long as possible. Mitigation of the ions (or in simpler terms: keeping the ionic debris away from the mirror surfaces) has therefore remained a primary challenge in developing an economical EUV light source. Currently, a substantial research effort is focused on ion mitigation schemes such as introducing a buffer gas into the vacuum chamber to decelerate and stop ions [22, 23], or magnetic fields to deflect ions away from the optics [24, 25]. However, few efforts have been devoted to properly characterizing and modelling the evolution of ion populations during the expansion. This shift in approach could advance the development of ion mitigation schemes for commercial systems, and may provide better insight into the relevant physics at play.

1.3 Project motivation

At ARCNL, we aim to understand the properties of the tin LPP expansion by characterizing (i) the number of ions generated in the expansion (ii) the charge state Z of the detected ions and (iii) their respective kinetic energies. In recent experiments, it has been found that the ion charge state Z detected in the experiments exhibits a consistent power-law dependence on the ion kinetic energy. In other words, higher charge states move faster. This is found through measurements of the distribution of ion kinetic energies recorded under various angles. The surprising finding here is that the power-law behavior is invariant under all angles of detection, and even widely varying laser parameters. This project aims to provide theoretical insights to explain this behavior, which, as of yet, cannot be reproduced by radiation-hydrodynamic simulations. This is because the simulations calculate the average charge Z (which is taken from tables) in local thermal equilibrium with no time dependence.

To do so, we address an important yet missing piece of the puzzle: *a theoretical account of recombination processes in the plasma expansion*[1]. Recombination is the process through which ions in a plasma reduce their charge state by capturing and retaining free electrons. A study of this phenomenon in the context of tin LPPs relevant to EUV lithography is the overarching theme of this report. This involves identifying the dominant recombination process occurring in the expansion (either radiative, three-body or dielectronic), as well as figuring out (i) when and (ii) where the average charge state "freezes", or no longer evolves. These findings will then be coupled with the prediction of the radiation-hydrodynamic simulations to explain the experimentally observed invariance of charge state as function of kinetic energy.

This report is structured as follows. First, in Chapter 2, we will give an overview of the recent experimental and modelling work on ion characterization at ARCNL including the charge-state energy spectrum measurements. In Chapter 3, we will discuss the various recombination mechanisms and identify the dominant process in the expansion phase of the LPP. Next, a numerical model is devised to quantify the effect of recombination on ion populations in Chapter 4. Here, we will also make the connection between the effect of recombination and charge state freezing, and the invariance of the average charge state spectrum. This is followed by a discussion and outlook in Chapter 5.

[1] Although recombination in expanding LPPs has been studied in literature [26, 27, 28, 29, 30], little recombination modelling has been done specific to the plasmas at ARCNL.

2 Recent ion characterization

In this Chapter, the ongoing efforts of characterizing the ions in the plasma expansion are briefly summarized. At ARCNL, these results are currently obtained through a combined effort of both experiment and simulation. First, we highlight some key aspects of the experimental approach and set-up, and discuss measurements relevant to this work. Thereafter, we discuss a radiation-hydrodynamic simulation code, RALEF-2D [31], which helps us understand the ions in terms of mass flow (how much material is moving at what energy). Finally, we discuss both the overlap and discrepancies in results obtained by the two intrinsically different approaches.

2.1 Ion energy spectroscopy

Here, we briefly review the experimental work done by Poirier *et. al.* [32, 33, 34] at ARCNL, where the individual charge-state-specific kinetic-energy distributions of tin ions produced by an LPP have been obtained using retarding field analyzers (RFA). Opposed to other diagnostic tools such as *e.g.* electrostatic probes [35] or electrostatic analyzers [33, 36], RFAs are well-suited to obtain angle-dependent measurements around the LPP being more compact and easier-to-align devices. The RFA method is schematically depicted in Fig. 2.1.

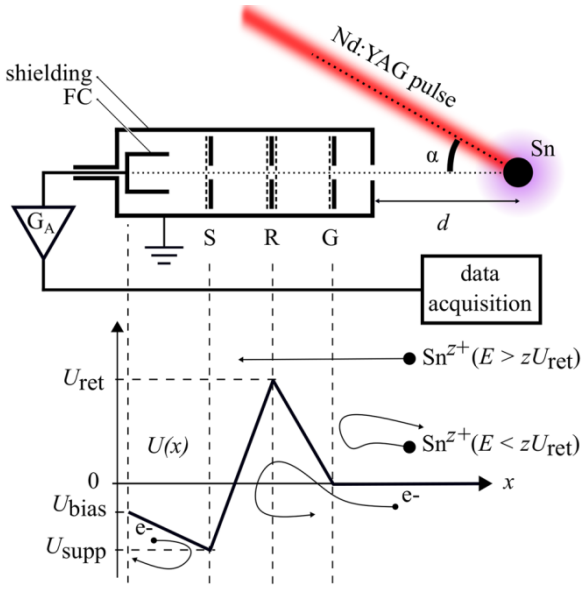

Figure 2.1: Schematic of RFA placed at an angle α with respect to the incoming laser pulse on the target. The potentials correspond to the various grids in the RFA, which can be tuned to resolve specific charge states. Taken from Ref. [32].

As is seen in Fig. 2.1, the RFA contains four grids through which the ions created in the plasma pass: a grounding grid (G), two retarding grids (R) and a suppressor grid (G) before arriving at the shielding Faraday cup (FC). By varying the retarding voltage U_{ret} between 10 and 500 V in steps of 20 V, one is able to generate a potential barrier which can repel ions of charge Sn^{Z+} of energy $E < ZeU_{\mathrm{ret}}$. Using the FC, it is checked that the ion current drops to zero at the maximum voltage so all ions are rejected. A more detailed discussion of the experimental set-up can be found in Ref. [32].

2.1.1 Data processing

The RFA measurements are obtained in the form of time-of-flight current traces $\frac{\partial^2 Q}{\partial t \partial \Omega} \approx \frac{\mathrm{d}Q}{\mathrm{d}t}\frac{1}{\Delta\Omega}$, which can be averaged over the small solid angle $\Delta\Omega$. The measurements can subsequently be converted to energy spectra $\frac{\mathrm{d}Q}{\mathrm{d}E}$ by dividing the current traced into n energy bins of width eU_{ret}:

$$\frac{\mathrm{d}Q}{\mathrm{d}E} = \frac{\mathrm{d}Q}{\mathrm{d}t}\frac{\mathrm{d}t}{\mathrm{d}E} \Longrightarrow Q_n(E_n) = \int_{neU_{\mathrm{ret}}}^{(n+1)eU_{\mathrm{ret}}} \frac{\mathrm{d}Q}{\mathrm{d}E}\mathrm{d}E. \tag{2.1}$$

As is seen, the corresponding bins have the boundary values neU_{ret} and $(n+1)eU_{\mathrm{ret}}$, such as to be centered around $E_n = (n+1/2)eU_{\mathrm{ret}}$. This way, the n-th bin contains contributions from charge states $Z = 1, .., n$. Subsequent ions with a charge state $Z = n+1$ will pass the R grid (see Fig. 2.1) as to end up in the $(n+1)$-th bin. This is also captured in the following expression $Q_n = \sum_{Z \leq n} Q_n^Z$, from which the charge-state-specific energy spectra can be obtained through

$$\frac{\mathrm{d}Q^Z}{\mathrm{d}E} = \frac{\mathrm{d}Q_{n=Z}}{\mathrm{d}E} - \frac{\mathrm{d}Q_{n=Z-1}}{\mathrm{d}E}. \tag{2.2}$$

The measured charge-state resolved ion energy spectra are plotted, for a sample case, in Fig. 2.2, including the total charge-integrated energy spectrum (solid red). It can be seen that the higher charge states attain higher peak kinetic energies, each followed by an exponential drop after having reached the peak energy. The charge-integrated spectrum (black dotted line) can be characterized by a near-constant region between 0.03-1 keV followed by a distinct peak around 2 keV. This peak can be attributed to the formation of a quasi-spherical expanding shell early on in the expansion [37]. The limited range of included charge states ($Z = 1-8$) is due to a combination of limitations of the detection method, and recombination taking place.

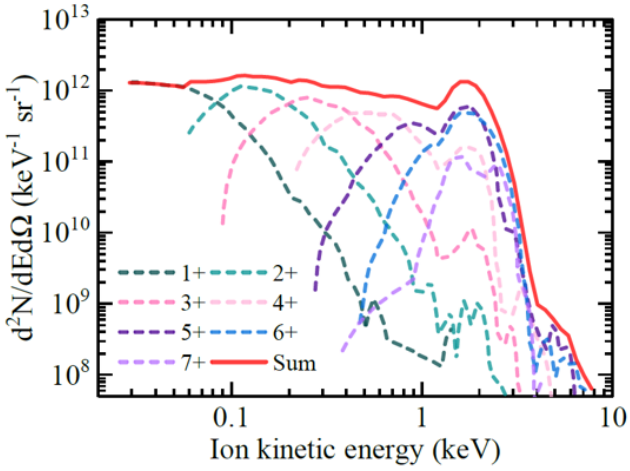

Figure 2.2: A sample of a charge-state-resolved ion energy spectrum taken with an RFA with the sum of the different charge states Sn^{Z+} with $Z = 1-8$ (solid red). Taken from Ref. [32].

2.1.2 Average charge state vs. energy: $\bar{Z}(E)$ invariance

Using the recorded charge-resolved ion energy spectra, we can also obtain the energy spectrum of the average charge $\bar{Z}$. For this, we compute the average charge in the following way:

$$\bar{Z}(E) = \frac{\sum_Z Z \frac{\mathrm{d}N}{\mathrm{d}E_Z}}{\sum_Z \frac{\mathrm{d}N}{\mathrm{d}E_Z}}. \tag{2.3}$$

First, the measured $\frac{\mathrm{d}Q}{\mathrm{d}E}$, e.g. from Fig. 2.2, is converted to the number of ions per charge state using $\frac{\mathrm{d}N}{\mathrm{d}E_{\mathrm{tot}}} = \frac{\mathrm{d}Q}{\mathrm{d}E_{\mathrm{tot}}}/(e\bar{Z})$. From Eq. (2.3) can be seen that the $\bar{Z}(E)$ graph can be determined by essentially taking the average of the charge-resolved $\frac{\mathrm{d}N}{\mathrm{d}E_Z}$ at each energy step. We now turn to Fig. 2.3 for an example of these $\bar{Z}(E)$ graphs. All 4 measurements were done with a 1 µm MP laser. The FWHM of the (Gauss) spatial and temporal profiles were 100 µm and 6 ns, respectively. The droplet was 17 μm in diameter. Here, the (total) ion kinetic energy distributions recorded under various angles α, and laser energies are plotted in the first seven figures. The final figure on the bottom right shows the average charge $\bar{Z}(E)$ plotted against kinetic energy for all above cases. The result is perhaps surprising: for all angles of detection, the average charge $\bar{Z}$ exhibits a similar power-law dependence on the kinetic energy. In other words, higher charge states move faster. Note that the energy spectrum is not fully invariant of the used laser pulse energy, as it still determines the highest ion energy cut-off.

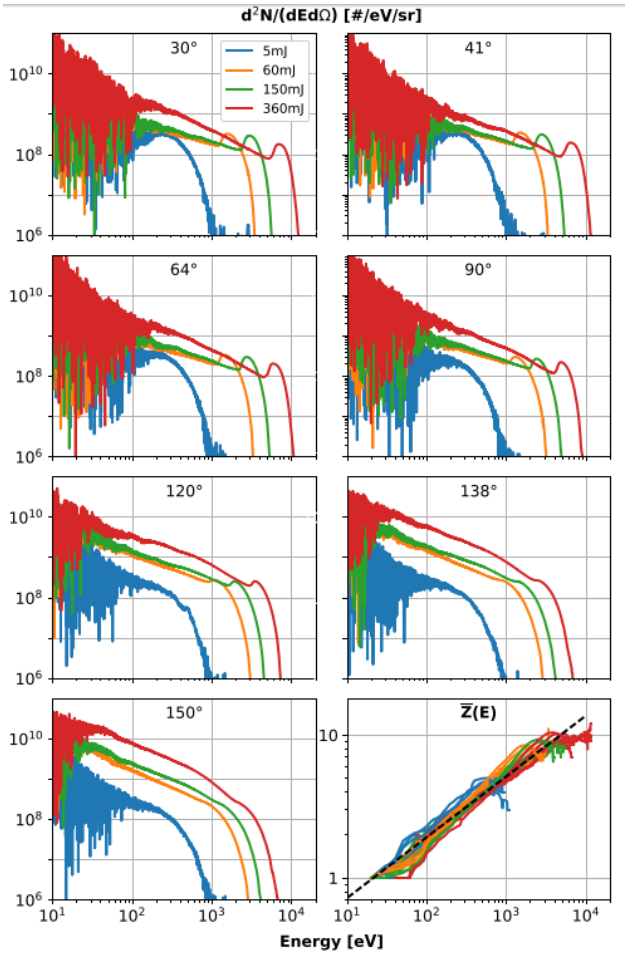

Figure 2.3: Four different ion energy spectra measurements with 7 individual RFAs at various angles. $Z(E)$ for all 28 cases is seen in the last box.

Over the past years, a large number of RFA measurements has been recorded for a wide range of experimental parameters to further investigate this $\bar{Z}(E)$ invariance. This includes different spatio-temporal laser profiles (Gaussian, box), laser energies, PP + MP schemes and different measurement angles α. The resulting $\bar{Z}(E)$ graphs for 276 different cases are shown in Fig. 2.4. It can be clearly seen that the $\bar{Z}(E)$ graphs persist to show the same repetitive trend.

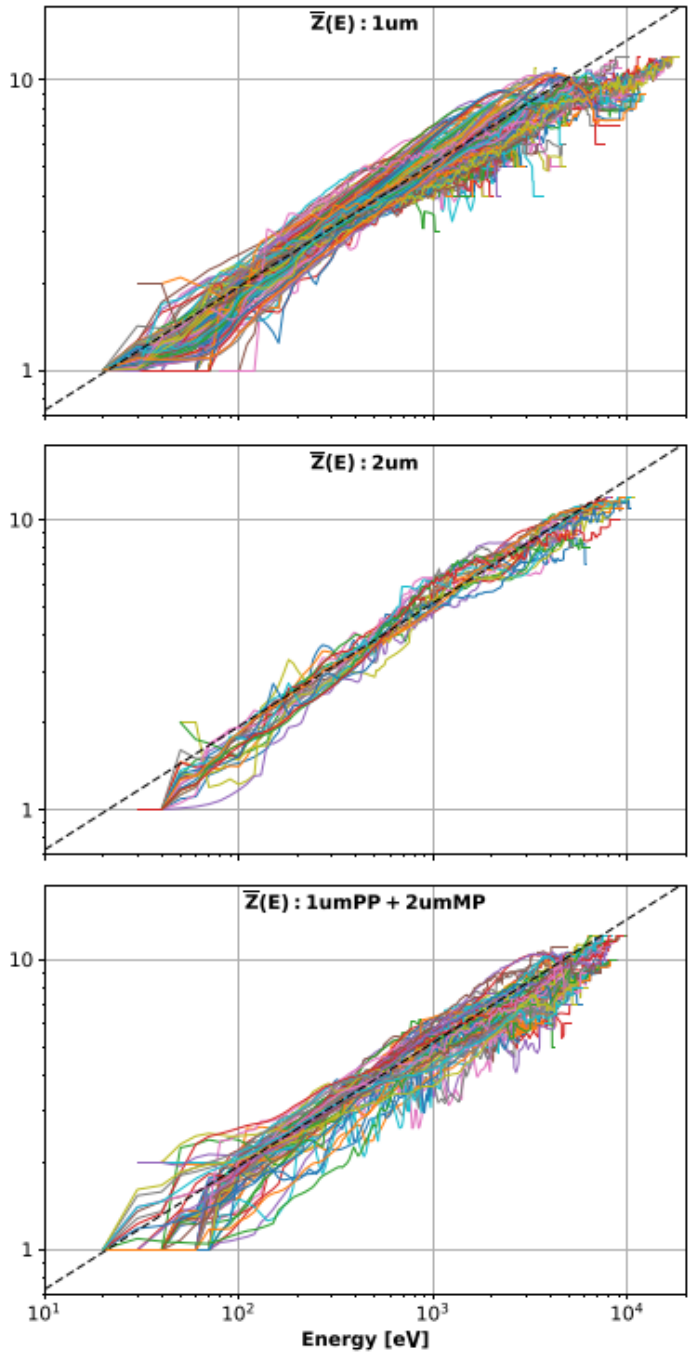

Figure 2.4: Average charge state $\bar{Z}$ against ion kinetic energy for the measurements from 1 μm laser (top panel), 2 μm laser (middle panel) and 1 μm (PP) + 2 μm (MP) scheme (bottom panel).

It is useful to further analyze this recurring trend of the data. By averaging over the complete collection of measurements from Fig. 2.4, it was found that the general trend can be fitted with a power-law of the form:

$$Z \propto E^{0.368} \tag{2.4}$$

As of yet, the best explanation for this power-law behaviour is a combination of the fact that the characteristic ion energy is proportional to the charge state and the electron temperature:

$$E \propto ZT_e, \tag{2.5}$$

This is supported by both Mora [38] and Murakami *et. al.* [39]. The two papers come to different final equations for E, but in both cases the proportionality can be reduced to Eq. (2.5). In addition, Basko *et. al.* found that a thermodynamically consistent power-law approximation can be applied to the tin equation-of-state in Ref. [40]:

$$Z \propto T^{0.6}. \tag{2.6}$$

By combining Eq. (2.5) and Eq. (2.6) in the following way

$$Z \propto \left(\frac{E}{Z}\right)^{0.6} \longrightarrow Z \propto E^{0.375}, \tag{2.7}$$

it is evident that this theoretical prediction is approximately in line with the power-law fit from Eq. (2.4). Nevertheless, the thing still lacking is more insight into the physical processes at play, as well as a more rigorous justification for the EOS approximation used in Ref. [40].

2.2 RALEF-2D

In this section, we give a short overview of some of the work done by Hemminga *et. al.* [37, 41] on plasma modelling. To elucidate the dynamics in the expansion phase as well as the ion energy distribution, the tin LPP is modelled using the code Radiative Arbitrary Lagrange–Eulerian Fluid dynamics in two dimensions (RALEF-2D). More specifically, this code treats the plasma containing free electrons and various ion species as a single-temperature, single fluid (which implicitly assumes quasi-neutrality in the plasma) and includes the effects of thermal conduction and radiation transport. RALEF-2D obtains the dynamics through solving the following hydrodynamic equations in 2D on a Cartesian, or radially symmetric mesh grid:

$$\frac{\partial \rho}{\partial t} + \nabla \cdot (\rho \mathbf{v}) = 0 \tag{2.8}$$

$$\frac{\partial (\rho \mathbf{v})}{\partial t} + \nabla \cdot (\rho \mathbf{v} \times \mathbf{v}) + \nabla p = 0 \tag{2.9}$$

$$\frac{\partial (\rho E)}{\partial t} + \nabla \cdot (\rho E + p)\mathbf{v} - (S_T + S_R + S_{\text{ext}}) = 0. \tag{2.10}$$

Here, the fluid is characterized by a mass density ρ and fluid velocity $\mathbf{v}$. Furthermore, p denotes the pressure, $E = E_{\text{int}} + E_{\text{kin}} = E_{\text{int}} + \frac{1}{2}|\mathbf{v}|^2$ the total mass-specific energy, S_T the thermal conduction, S_R the heating rate for a specific volume due to thermal radiation and S_{ext} external energy sources (think of laser beam energy). In this single-fluid model, the ion number density n_i and electron number density n_e are related by the average charge $\bar{Z}$ through $n_e = \bar{Z} n_i$. RALEF-2D is still able to resolve the average charge states for a given mass density and temperature in this single-fluid approach by assuming an equation-of-state (EOS).

In this hydrodynamic formalism, the gradients in the plasma pressure drive the plasma expansion. The validity of this approach is, however, dependent on whether the local Debye length $\lambda_D = \sqrt{T_e/(4\pi n_e e^2)}$ is significantly smaller than the length scale of variations in the flow $L = n_i/|\nabla n_i|$. Usually, this condition is met in the hot and dense regions of the plasma, just after being formed. As the plasma expands into the vacuum, however, the hydrodynamic description may lose its predicting abilities.

2.2.1 Comparison between experiment and simulation

To demonstrate how the simulation results from RALEF-2D concerning the charge-integrated ion energy spectrum compare to the experimental measurements from Sec. 2.1, we turn to Fig. 2.5. It is immediately evident that the results from experiment and simulation closely resemble each other. RALEF-2D is able to reproduce most qualitative features such as the near-plateau between 0.1-1 keV, the high-energy peak located at 2 keV and the exponential drop-off for energies higher than 2 keV. Figure 2.5 also clearly shows that the simpler analytical models from Mora [38] and Murakami *et. al.* [39] are not able to reproduce the experimentally recorded spectra, the most notable difference with RALEF-2D being that the density profiles adopted in these models are oversimplified. In a more recent paper by Poirier *et. al.* [34], the same overlap between experiment and simulation has been found for spectra recorded under various angles from the target.

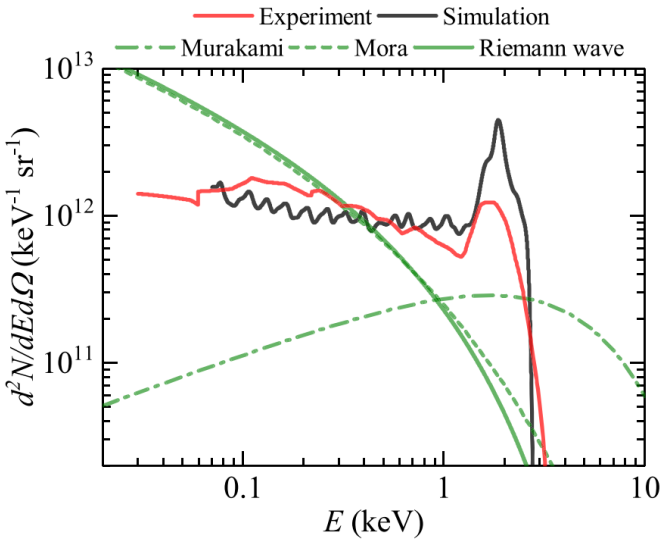

Figure 2.5: Ion number distributions against kinetic energy. The experimental measurements and simulation results from RALEF-2D are shown respectively by the red and black curves. Also shown are the predictions from Refs. [38, 39].

For a complete discussion on the validity of RALEF-2D as well as the remaining discrepancies between experiment, we refer to Ref. [37]. Here, however, we would like to highlight one possible cause that could contribute to the observed difference between experiment and simulation. We suspect that this is also the reason for RALEF-2D to not be able to reproduce the $\bar{Z}(E)$ invariance. It concerns the EOS model adopted in the work from Ref. [37], which assumes local thermal equilibrium (LTE) ionization over the full simulated domain. This assumption is known to break down later in the expansion when recombination processes become negligible, *i.e.* the charge state freezes out (this phenomenon will be discussed in more detail in Chapter 3). The length scale associated with this freezing effect thus determines how much of the spatial domain can be accurately simulated using the hydrodynamic approach employed by RALEF-2D. In Chapters 3 and 4, we will investigate the effect of recombination and charge state freezing in more detail.

3 Plasma recombination theory

Plasma recombination plays a crucial role in determining the ionization balance of an expanding plasma, being responsible for reducing the charge state of ions. In the previous Chapter, it became evident that recombination, as of yet, is not explicitly accounted for in RALEF-2D and hence could explain at least part of the discrepancies between ion characterization by experiment and simulation. In this Chapter, we introduce the relevant physics behind plasma recombination and discuss the ways in which we can model various recombination mechanisms.

3.1 Different recombination mechanisms

Generally speaking, ions can drop in charge state by undergoing a recombination process. Such a process involves a positively charged ion that captures and retains a free electron, which can happen in several distinct ways. Here, we will discuss three recombination processes (radiative, three-body and dielectronic), and include a discussion on the rates at which these processes occur and on what plasma parameters the rates depend.

3.1.1 Radiative recombination

Radiative recombination (RR) refers to the process where an incoming, free electron is captured by a positively charged ion, and the energy difference is accounted for by the emission of a photon of frequency ν. This can also be captured in the following way (see also Fig. 3.1):

$$\mathrm{Sn}^{+Z} + \mathrm{e}^- \rightarrow \mathrm{Sn}^{+(Z-1)} + h\nu. \tag{3.1}$$

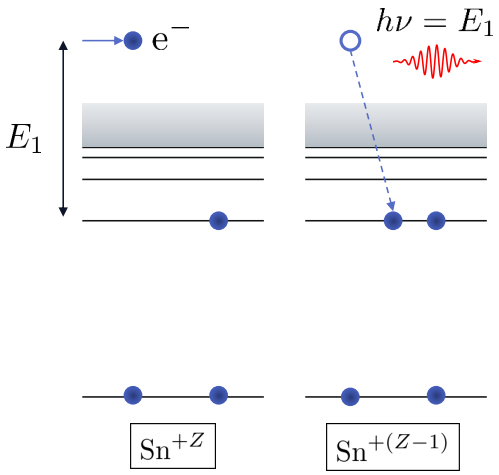

Figure 3.1: Schematic representation of the radiative recombination process.

To model a recombination mechanism, the rate is often captured using so-called rate coefficients in units of cm^{-3}. This makes constructing a rate equation with ion populations, which are usually taken per given volume, more straight-forward. The rate coefficient for the radiative recombination mechanism is taken from Refs. [42, 43, 44]:

$$\alpha_Z^{\mathrm{RR}} = 5.2 \cdot 10^{-14} \sqrt{\frac{I_Z}{T_e}} Z \left(0.429 + \frac{1}{2} \log \frac{I_Z}{T_e} + 0.469 \sqrt{\frac{T_e}{I_Z}} \right), \tag{3.2}$$

where I_Z is the ionization potential for charge state Z. The formula for recombination of an electron and ion is obtained by manipulation of an analytical expression to fit the asymptotic expansion of the Kramers-Gaunt factor containing three terms. In essence, it represent an empirical fit to a collection of experimental data. Although a crude approximation, the expression in Eq. (3.2) is still widely used in modelling of ionization balances to this day, *e.g.* Ref. [30].

3.1.2 Three-body recombination

A different recombination process is three-body recombination (TBR), also referred to as collisional recombination. The energy released in the capturing of a free electron is directly transferred to a second free electron. In a way, the process is similar to radiative recombination, but with the third body being an electron rather than a photon. This radiation-less process can be captured in equation-form as well the schematic in Fig. 3.3:

$$\mathrm{Sn}^{+Z} + \mathrm{e}^- + \mathrm{e}^- \rightarrow \mathrm{Sn}^{+(Z-1)} + \mathrm{e}^-. \tag{3.3}$$

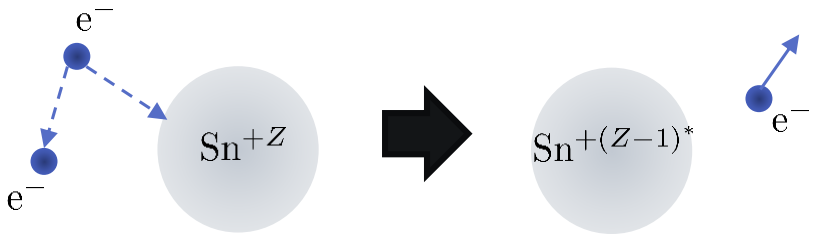

Figure 3.2: Schematic representation of the three-body recombination process.

The rate at which the TBR process occurs brings up a point of discussion as there seems to be no real consensus on which approximation formula should be used. If we follow Refs. [42, 44, 45, 46], the rate coefficient can be approximated by the following expression:

$$\alpha_Z^{\mathrm{TBR}} = 2.97 \cdot 10^{-27} \xi_Z / T_e I_Z^2 \left(4.88 + \frac{I_Z}{T_e} \right), \tag{3.4}$$

where ξ_Z denotes the number of electron in the outermost shell of charge state Z. Alternatively, if we consider the work described in Refs. [26, 27, 30, 47, 48] the rate coefficient is given by

$$\alpha_Z^{\mathrm{TBR}} = 8.75 \cdot 10^{-27} \frac{\bar{Z}^2 n_e^2}{T_e^{9/2}}. \tag{3.5}$$

Crucial to this second expression is the strong inverse scaling with the electron temperature of $T_e^{-9/2}$. To get a better grasp on how this expression comes about, we recapitulate the arguments presented in Ref. [48]. Here, recombination is regarded as a diffusion process in the direction of negative energies for an electron bounded in its motion by the electric field of the charge particle.

Rather than considering the full atomic structure, it is assumed that (in the low-temperature case) recombination occurs primarily through channels in the upper levels such that the spectrum becomes continuous. So it is argued that the capturing of electrons can be described classically by a kinetic equation, specifically an electron distribution function that is written in the Fokker-Planck form. The expression is valid for relatively low-temperature plasmas $k_B T_e \ll I_Z$ at high densities. For further details, we refer to Ref. [48].

3.1.3 Dielectronic recombination

Among the most challenging recombination processes to model is dielectronic recombination (DR). The difficulty arises from the fact you have to know the full atomic structure of the target state, which for heavy Sn ions is extremely challenging. This makes accurate calculation of the process very difficult. In dielectronic recombination, the energy which becomes available during the capture of a free electron is directly given to the promotion of a bound electron to a higher bound orbit, which leads to a doubly excited state. Subsequently, the atomic state relaxes to a lower-lying state which leads to the emission of a photon. Thus, dielectronic recombination is distinctly a two-step resonant process captured in equation-form and in Fig. 3.3.

$$\mathrm{Sn}^{+Z} + \mathrm{e}^- \rightarrow \mathrm{Sn}^{+(Z-1)**} \rightarrow \mathrm{Sn}^{+(Z-1)} + h\nu \tag{3.6}$$

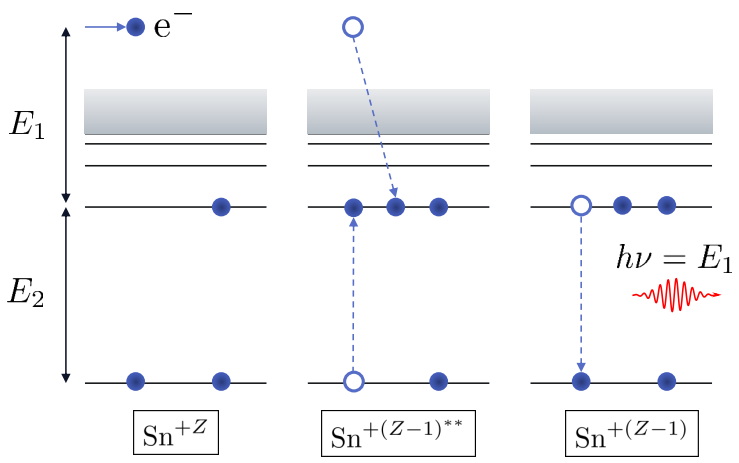

Figure 3.3: Schematic representation of the dielectronic recombination process.

The DR rate coefficient has been notoriously hard to calculate because it involves doubly excited states, or (if you have strong mixing of states) even triply excited states. For this reason, previous work has used either approximate formulations (scaling laws similar to Eqs. (3.2) and (3.4)) or has fully neglected DR in collisionial-radiative models. Now, to account for the DR process, we will utilize the detailed atomic calculations of Badnell *et. al.* [49] via the $4p^6 4d^q - 4p^6 4d^{q-1} 4f + 4p^5 4d^{q+1}$ transition arrays for $q = 1 - 10$. The paper uses three approaches to do so of varying degrees of complexity: (i) configuration-mixed level-resolved Breit-Pauli using autostructure, (ii) bundled-nl using the Burgess-Bethe general program and (iii) configuration average using the DRACULA code, the details of which can be found in Ref. [49]. The resulting total rate coefficients (for all states stable against autoionization) for Sn^Z+ for $Z = 4 - 13$ are approximated using a functional form:

$$\alpha_Z^{\mathrm{DR}}(T_e) = T_e^{-3/2} \sum_k c_k \exp\left\{-\frac{E_k}{T_e}\right\}, \tag{3.7}$$

where E_k (in the units of temperature (eV)) and c_k (in units of $\mathrm{cm^3 s^{-1} (eV)^{3/2}}$) are fitting coefficients that can be found in Table 1 of Ref. [49]. The ion-specific DR rate coefficients are plotted against the electron temperature in Fig. 3.4, from which we can immediately infer the importance of the atomic calculations. It can be seen that the DR rate coefficients at high temperatures ($T_e > 80$ eV) follow a trend that could be captured in a simple functional dependence of Z and T_e. For lower T_e, however, the DR rate coefficient exhibits a non-uniform pattern of change in Z that becomes difficult to capture using analytical scaling laws. As eluded to before, this fact arises from the complexity of the underlying atomic structure and the resonant nature of the DR process, where the incoming electron must satisfy a resonance energy ($E_1 = E_2$) to promote a bound electron, as is illustrated in Fig. 3.3. This resonant character of the interaction is not present in RR and TBR.

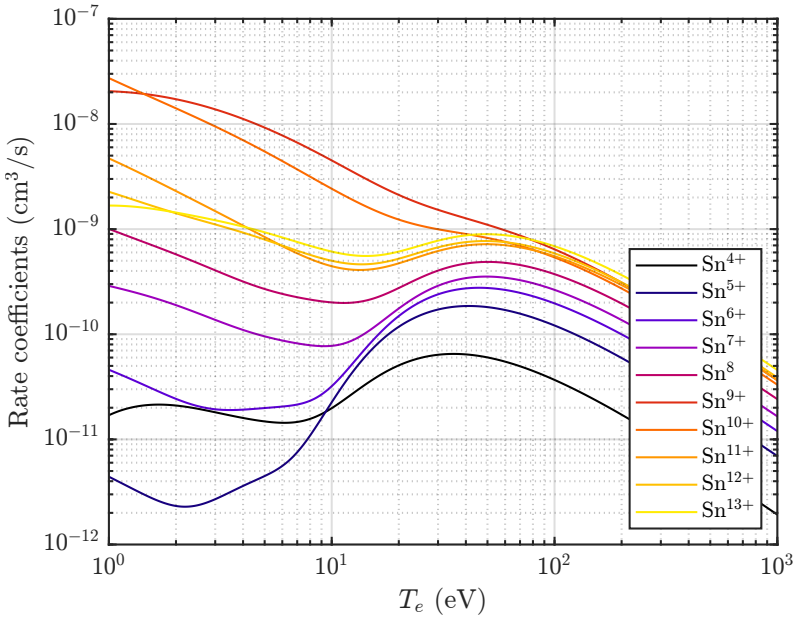

Figure 3.4: Dielectronic rate coefficients against electron temperature of Sn^{z+} for $z = 4 - 13$.

3.2 Comparing recombination rates

Next, we would like to identify the dominant recombination process for the temperatures and densities relevant to the tin LPPs used in EUV lithography. The expressions for the rate coefficients from Eqs. (3.2), (3.4) and (3.7) all have in common a dependence on the electron temperature T_e. Plotting the separate rate coefficients against T_e (see Figs. 3.5 and 3.6) thus makes for a good comparison tool. For example, we can estimate the relevant electron temperature range for an expanding tin LPP and subsequently determine which recombination process is most prevalent. Moreover, the lack of consensus on the TBR rate coefficient also motivates a further comparison.

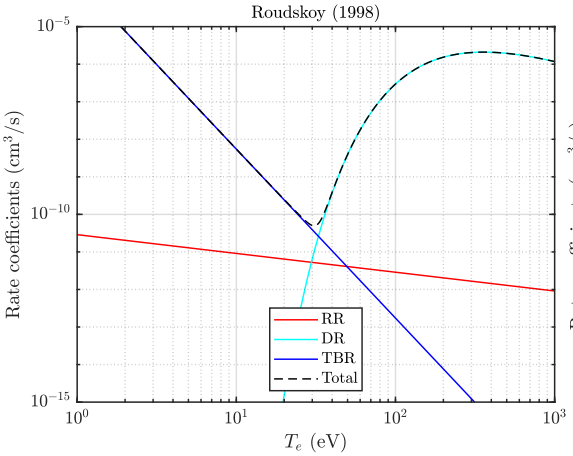

Figure 3.5: Rate coefficients against electron temperature (case 1).

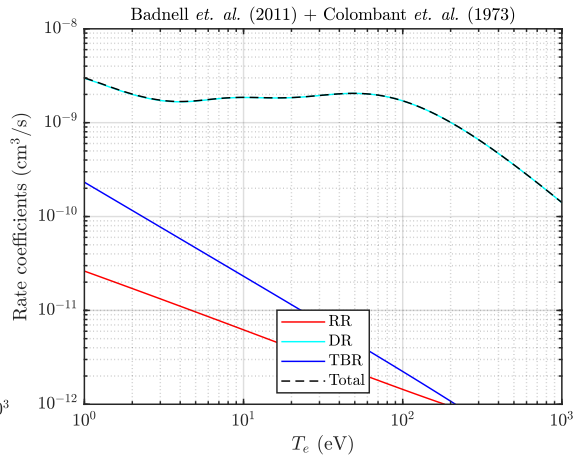

Figure 3.6: Rate coefficients against electron temperature (case 2).

In Fig. 3.5, we plot the rate coefficients of the various recombination mechanisms along with the sum against the temperature, specifically as given by Ref. [29]. It is important to note that here the DR rate coefficient is approximated using Burdgess' law and is *not* found through extensive atomic calculations. Plotting these coefficients against temperature reveals that DR is fully dominant for $T_e > 30$ eV, TBR fully dominates recombination for $T_e < 30$ eV and RR is negligible compared to the other mechanisms over the full temperature range. Here we stress that these insights, especially TBR being dominant in the low-temperature regime, have been leading in papers on the topic until now.

In Fig. 3.6, we plot again the rate coefficients for the various recombination mechanisms, but now we take the DR rate coefficients (for $Z = 7$) from Badnell *et. al.* [49] and the TBR and RR from Colombant *et. al.* [42]. It is immediately evident that this gives completely different results compared to the other rate coefficients. Most notable is the undisputed dominance of the DR process over the full temperature range. This results, in part, from the non-uniform pattern of change in the DR rate coefficients resulting from the complexity of the underlying atomic structure (see again Sec. 3.1.3). Further, the TBR rate coefficient from Ref. [42] has a significantly weaker inverse temperature dependence compared to Ref. [47] (see again Eqs. (3.4) and (3.5)) such that the TBR rate coefficient in Fig. 3.6 attains smaller overall values compared to Fig. 3.5. The reason for highlighting these differences is that, until now, almost all recombination models of tin LPP expansion (see Refs. [26, 27, 36, 30]) are based on the recombination rates taken from Roudskoy, and hence omit the new insights that the atomic calculations brought forth on the dominant role of the DR mechanism. This is particularly important for the temperature range $T_e < 30$ eV, because in the expansion phase, the plasma drops in electron temperature significantly. In Chapter 4, we will study the role of DR in the expansion phase in more detail.

3.3 Charge state freezing

An important effect closely tied to recombination is the so-called freezing of the charge state. This phenomenon occurs in regions where the plasma density and temperature are such that all recombination processes become negligible. This is especially of interest in highly ionized plasmas, where the moment of freezing can occur before all ions have fully recombined, which implies the final average charge state is greater than zero ($\bar{Z} > 0$). Moreover, we have already seen in Sec. 2.2 that the length scale of the freezing effect determines to what extent the hydrodynamic approach of RALEF-2D remains valid.

Following literature [26, 27, 29], the freezing effect is intrinsically tied to the nature of the TBR mechanism. It is argued that in the (adiabatic) plasma expansion, energy is lost due to work by the plasma pressure Q_{hyd}, but energy is *also* returned to the plasma as a small amount of energy E^* is released in each act of three-body recombination:

$$Q_{\mathrm{rec}} \sim \alpha^{\mathrm{TBR}} E^* \tag{3.8}$$

During the expansion, it occurs that Q_{hyd} becomes comparable in size with Q_{rec} such that the expansion ceases to be adiabatic. Following the derivation in Ref. [29], by constructing an electron energy balance, one can analytically solve for the asymptotic behaviour of the electron temperature T_e and the average charge $\bar{Z}$. For example, it is shown that the energy term resulting from the TBR mechanism Q_{rec} is responsible for shifting the temperature profile from $T_e \propto t^{-2}$ (adiabatic) to approximately $T_e \propto t^{-1}$. As the decrease in T_e is slowed significantly and the TBR rate is strongly dependent on T_e (see Eq. (3.5)), recombination effects become negligible and the average charge state can stop changing, *i.e.* $\bar{Z} \xrightarrow{t\to\infty}$ constant $\neq 0$. To connect this phenomenon to a length scale, a freezing distance can be computed by setting $Q_{\mathrm{hyd}} \sim Q_{\mathrm{rec}}$. This results in

$$r_{\mathrm{frz}} \propto \frac{T_e^{\frac{13}{12}} v_i^{\frac{14}{6}} \tau_l^{\frac{13}{6}}}{n_e^{\frac{8}{18}} d^{\frac{8}{6}}}, \tag{3.9}$$

where v_i is the ion speed, τ_l the laser pulse length and d the laser waist at the focus. We stress here that the author from Ref. [29] states that the numerical value of Eq. (3.9) is not of interest because a large number of assumption is made in getting to the expression, but the scaling with other parameters is interesting. For example, from the scaling with the ion velocity can be derived that faster ions begin to recombine further away from the target than slowly moving ions which reduces the loss in charge state. This might explain why more energetic ions have higher charge states.

We like to stress that the theoretical insights into charge state freezing resulting from the TBR mechanism presented here are still present in more recent literature, *e.g.* in Ref. [30] where it is even used to give numerical estimates of the freezing distance r_{frz}. The current literature on charge state freezing is, however, predicated on the fact that TBR is the only recombination process which should be accounted for. Our main concern is that, as of yet, the role of dielectronic recombination is omitted in the discussion on plasma expansion and charge state freezing, which is unjustified in light of the results from Badnell *et. al.* [49]. Moreover, the analytical expression from Eq. (3.9) cannot be employed to give accurate estimates of the freezing distance, but should rather be found through a more detailed numerical calculation. Hence, in Chapter 4, we will examine the role of both DR and TBR in the plasma expansion and freezing using a numerical model.

4 Numerical model of ion expansion

In this Chapter, the main results are presented on the effects of recombination in expansion of a tin LPP. To this end, a numerical model is devised to describe the evolution of various tin ion populations throughout the expansion phase. The proposed model includes the most recent data on dielectronic recombination, which was introduced in the previous chapter.

4.1 Time-dependent ion expansion model

A commonly used approach to simulate ion populations throughout the expansion is a collisional-radiative (CR) model [42]. As the name suggests, this type of model takes into account the collisional and radiative plasma processes of both recombination and ionization/excitation. We derive a numerical model similar in spirit to this to study the effect of recombination on ion populations in the expansion phase. We motivate this model by first revisiting two findings. First, the rate at which each recombination process (described in Chapter 3) occurs is heavily dependent on the electron plasma temperature T_e and electron density n_e. Second, both the electron temperature and density evolve significantly over time in the expansion phase of a laser-produced tin plasma. Consequently, we propose a model consisting of a set of $Z+2$ differential equations: one for each ion population N_Z that we take into account, one for the electron temperature T_e and one for the electron density n_e.

A specific charge state can be populated and depopulated through both recombination and ionization events, which is depicted in Fig. 4.1. One can keep track of the temporal evolution of a population (fraction) N_Z through a rate equation of the following form:

$$\frac{\mathrm{d}N_Z}{\mathrm{d}t} = n_e\left[\alpha^{\mathrm{tot}}_{Z+1}(T_e, n_e)N_{Z+1} - \alpha^{\mathrm{tot}}_{Z}(T_e, n_e)N_Z\right] \tag{4.1}$$

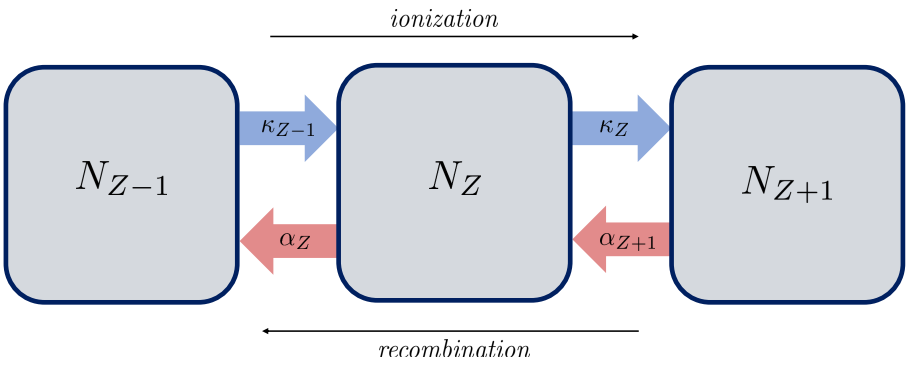

Figure 4.1: Schematic of rate equation approach to ion populations.

Here, the total charge-state-specific recombination rate coefficient α_Z^{tot} is given as the sum of the three distinct recombination processes:

$$\alpha_Z^{\mathrm{tot}} = \alpha_Z^{\mathrm{RR}} + n_e \alpha_Z^{\mathrm{TBR}} + \alpha_Z^{\mathrm{DR}}, \tag{4.2}$$

where the rate coefficients are respectively given by Eqs. (3.2), (3.4) and (3.7). Note that ionization processes are fully neglected in Eq. (4.1). This assumption is valid after plasma formation when the laser pulse has terminated, because the ionization potentials of the created highly charged ions ($Z > 7-8$) are very high and there are few high-energy electrons in the distribution with energies higher than the ionization potential. Especially without an additional source of energy in the expansion, this greatly reduces the probability of ionization events compared to recombination. If we set Eq. (4.1) equal to zero, and plug the ionization coefficients κ_Z back in, one retrieves the CR steady-state model from Ref. [42]. However, we go beyond the steady-state approximation and solve for time-dependent evolution. As we will study the plasma after termination of the laser pulse, the plasma expansion is assumed to be adiabatic such that the temperature drops off as $T_e \propto t^{-2}$. One can approximate the system as adiabatic as there is no external energy source when the laser is switched off. This is captured in differential form as

$$\frac{\mathrm{d}T_e}{\mathrm{d}t} = -2\frac{T_e}{t} + X_{3b}, \tag{4.3}$$

where $X_{3b} = -\frac{2}{3}E^* \frac{\mathrm{d}\bar{Z}}{\mathrm{d}t}\frac{1}{\bar{Z}}$ and E^* (given by (11) in Ref. [26]) represent the energy returning to the plasma due to the TBR mechanism. *This will only be the case when the TBR rate coefficient from Eq.* (3.5) *is used*, in all other cases (no TBR, TBR from Colombant *et. al.* [42]) $X_{3b} = 0$. For the differential equation of the electron density n_e, we follow the argument presented in Ref. [26]. Here, it states that while the electron-ion interactions (such as recombination) can affect the charge state evolution, it has little to no effect on the ion or electron density scaling. In a free expansion in three dimensions, we can simply require the density to follow $n_e \propto t^{-3}$ for an expanding plasma element. This translates to a differential equation of the from:

$$\frac{\mathrm{d}n_e}{\mathrm{d}t} = -3\frac{n_e}{t}. \tag{4.4}$$

By simultaneously solving Eqs. (4.1), (4.3) and (4.4), we can track the temporal evolution of each ion population through evaluation of the recombination rate coefficients at varying electron temperatures and density. The temporal profiles imposed on T_e and n_e are, to good approximation, representative of the adiabatic plasma expansion occurring in the lab.

4.2 Initialization

Before the model represented by Eqs. (4.1), (4.3) and (4.4) can be numerically solved, we have to turn our attention to finding the initial conditions. We first consider the initial time t_0 at the which the simulation is started. For this, we consider the fact that when a laser heats free electrons in the plasma, electrons transfer energy to the ions on the scale of the electron-ion thermalization time given by [30]

$$\tau_{ei} \approx 3.5 \cdot 10^8 \frac{A T_e^{3/2}}{\bar{Z} n_e \ln \Lambda}, \tag{4.5}$$

where A is the atomic mass in atomic mass units (for tin 118.7 amu) and $\ln \Lambda \approx 5$ represents the Coulomb logarithm [50]. As the expansion phase is the primary focus of this model, we initialize the model at a time $t_0 > \tau_{ei} \approx 1$ ns after the heating stage when the electrons and ions are in thermal equilibrium. Since the model has no spatial dependence and therefore intrinsic geometry built in, we can assume a homogeneous, spherically symmetric plasma with a radius equal to the laser radius at the focus [51]. Next, for the model to yield reliable results, an accurate initialization at $t = t_0$ of all $Z+2$ variables is key. This consist for a large part of determining the

initial fractional ion populations $N_Z(t = t_0)$ at a specific initial electron temperature and density. Furthermore, it is logical to assume that the initial electron density $n_e(t = t_0)$ is approximately equal to the critical density n_{crit}. This critical density is relevant for the absorption of laser power via the process of inverse bremsstrahlung [11], and equals 10^{19} cm^{-3} for 10 μm CO_2 laser and 10^{21} cm^{-3} for 1 μm Nd:YAG lasers.

ATOMIC code

To find the initial ion population fractions $N_Z(t = t_0)$, we employ the ATOMIC code of which the details can be found in Refs. [19, 52]. This code takes into account all relevant data on the atomic structure of tin such as electronic configurations, ionization potentials, oscillator strength and more. This atomic data has been bench-marked with experimental data in Ref [20]. By explicitly considering all relevant collisional and radiative processes, the atomic species are then embedded in a plasma environment from which the level populations within atoms can be determined. This code specifies the plasma environment with a mass density ρ and electron temperature T_e to compute the level populations in either local thermal equilibrium (LTE) or non-local thermal equilibrium (non-LTE) conditions. In LTE, the code employs an equation-of-state (EOS) from ChemEOS to derive both the level populations and charge-state distributions [53]. A neat feature of this code is that it can provide accurate initial conditions for a wide range of densities and temperatures. This, in turn, enables us to employ the numerical model for a wide range of plasma conditions as well. The finer details of this code exceed the scope of this report, but can be found in Ref. [19].

To give an example of the calculated charge state distribution from ATOMIC, we turn to Fig. 4.2 where the relative populations are plotted against ion charge state for 9 different atomic codes. For an initial density $n_e(t = t_0) = 10^{19}$ cm^{-3} and temperature of 30 eV, the ion charge distribution is strongly peaked around $Z \approx 11$ in all cases. These populations can then be used as input $N_Z(t = t_0)$ for the numerical model described in Sec. 4.1. For the purposes of this report, we only utilize the output data of ATOMIC.

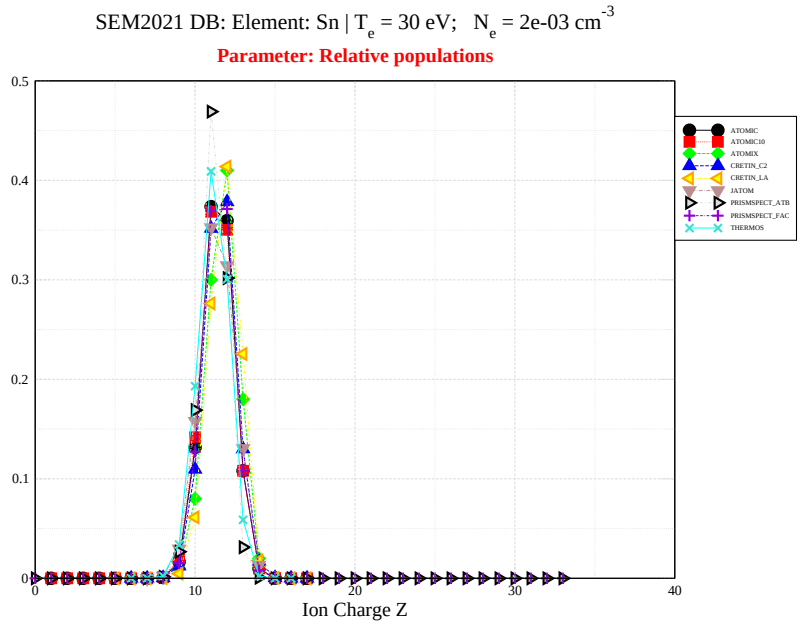

Figure 4.2: Initial fractional ion populations at $t = t_0$.

4.3 Simulation results

In this section, we obtain the temporal evolution of the ion populations under the influence of recombination effects by numerical integration of Eqs. (4.1)-(4.4) using a fourth-order Runge-Kutta scheme. First, we discuss the typical model output for a sample case. The goal here is to mainly show how the output data is analyzed on the hand of an example. After that, we run the model for a range of initial conditions and identify more general trends.

4.3.1 Evolving ion populations and average charge state

We start by demonstrating a typical result of the ion expansion model from Eqs. (4.1)-(4.4) for $T_e(t_0) = 30$ eV, $n_e(t_0) = 10^{19}$ cm^{-3} and the initial fractional populations from Fig. 4.2. In Fig. 4.3, the electron temperature (left) and density (right) are both plotted against time. As expected, the temporal profile of the temperature and density respectively fall of with t^{-2} and t^{-3} in accordance with the differential formulation in Eq. (4.3) and Eq. (4.4). The fractional ion populations of every charge state in the range $Z = 3 - 13$ is plotted against time as well in Fig. 4.4. It is clear that the fractional ion populations vary a lot over a duration of approx. 30 ns, after which the populations stabilize.

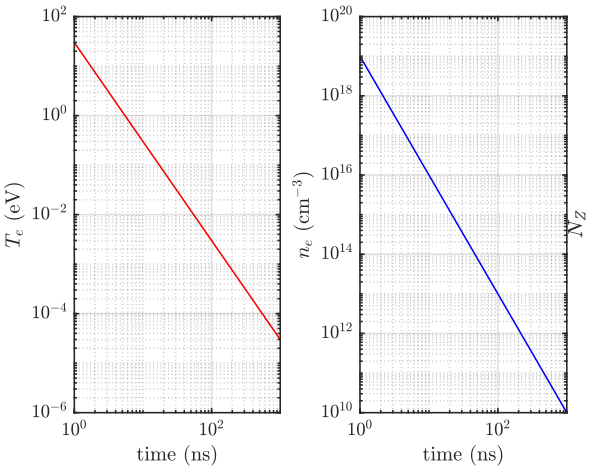

Figure 4.3: Electron temperature (left panel) and electron density (right panel) against time.

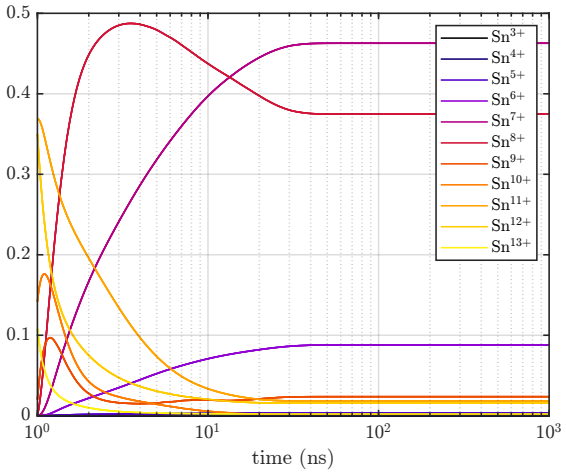

Figure 4.4: Fractional ion populations ranging from Sn^{3+} to Sn^{13+} against time. Colors denote different charge states.

Motivated by our interest in the evolution of the *average* charge state during the expansion (see Chapter 3), we can aggregate the individual fractional populations by simply computing $\bar{Z} = \sum_Z N_Z Z$ at every simulated time-step. The resulting graph is seen in Fig. 4.5, where the average charge is plotted against time. The code is also very flexible in "turning on/off" of distinct (combinations of) recombination mechanisms. In order to distinguish between distinct recombination processes for this specific example, we plot the evolution of $\bar{Z}$ for two cases: i) dielectronic recombination, (ii) dielectron recombination and three-body recombination (according to Eq. (3.4)). From this, we can establish that dielectronic is of great importance in determining the ionization balance, and the addition of TBR to the model only slightly reduces the average charge.

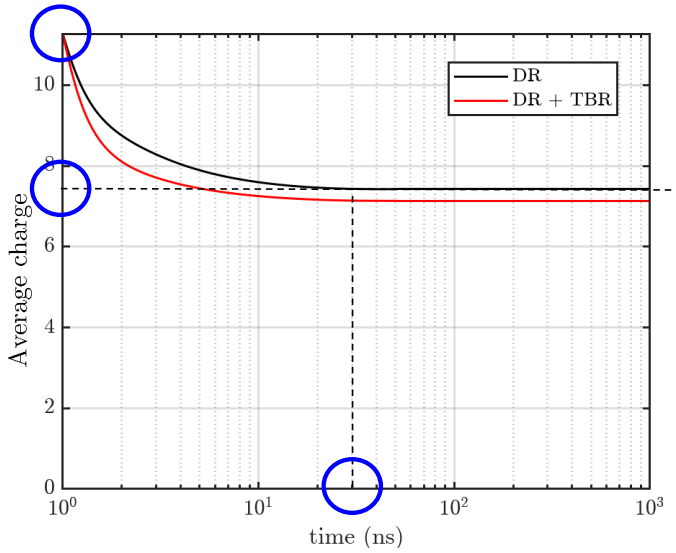

Figure 4.5: Average charge against time for DR (black) and DR/TBR (red).

Based on Fig. 4.5, we will now define a couple figures of merit that will be used for further analysis.

- The initial average charge $\bar{Z}_0 = \bar{Z}(t = t_0)$. This is determined using the ATOMIC10 code, as described in Sec. 4.2. For the example case in Fig. 4.5, $\bar{Z}_0 \approx 11$.
- The freezing average charge $\bar{Z}_{\text{frz}}$ taken as the value of $\bar{Z}$ which has stabilized in time. For the example case in Fig. 4.5, $\bar{Z}_{\text{frz}} \approx 7$.
- The freezing time t_{frz}. For the example case in Fig. 4.5, $t_{\text{frz}} \approx 30$ ns.

Conveniently, the freezing time t_{frz} can be converted to a freezing distance d_{frz} if we assume that the boundary of the initial domain expands spherically for all time at a constant speed approximately equal to the plasma sound speed. The plasma sound speed is given by

$$c_{s,0} = \sqrt{\frac{5\bar{Z}_0 T_{e,0}}{M_i}}, \tag{4.6}$$

where M_i denotes the ion mass. The time-to-space conversion is then simply done by $r_{\text{frz}} = c_{s,0} t_{\text{frz}}$. If we compare the freezing time of $t_{\text{frz}} \approx 30$, this translates to a freezing distance r_{frz} of around 200-300 μm. We again stress that above results are specific to the initial conditions of the example, in this case relevant to industrial CO_2-laser system. In the next section, we will explore a broader range of initial conditions.

4.3.2 Range of initial conditions

Now, we will solve the ion expansion model for a range of initial temperatures ($T_{e,0} = 10 - 50$ eV in 5 eV increments) and densities ($n_{e,0} = 10^{19}$, 10^{20}, 10^{21} cm^{-3}). The corresponding initial ion populations for every combination of n_e, T_e are found by employing the ATOMIC code[1]. From each simulation, we store the values of $\bar{Z}_0$, $\bar{Z}_{\text{frz}}$ and t_{frz}. In what follows, we plot the freezing average charge against the initial average charge using different combinations and expressions for recombination rate coefficients along with linear fits.

[1]Since the DR rate data is only available for $Z = 3 - 13$, this sets a limited range for the number of charge states included in the model. For some combinations of temperature and density, however, the value for $\bar{Z}_0$ was too high to be accurately represented by the model. Hence, these results are not presented.

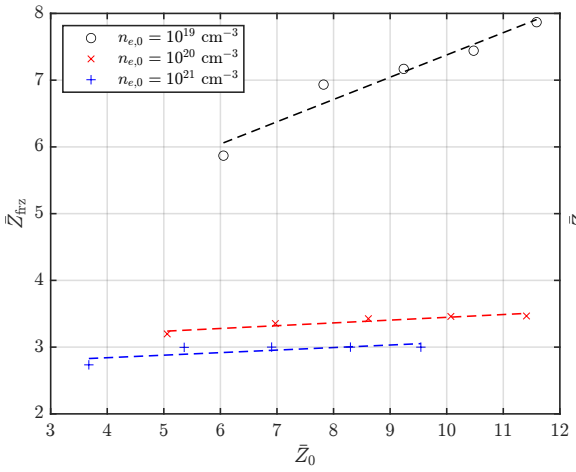

Figure 4.6: Freezing average charge against initial average charge, only taking into account DR.

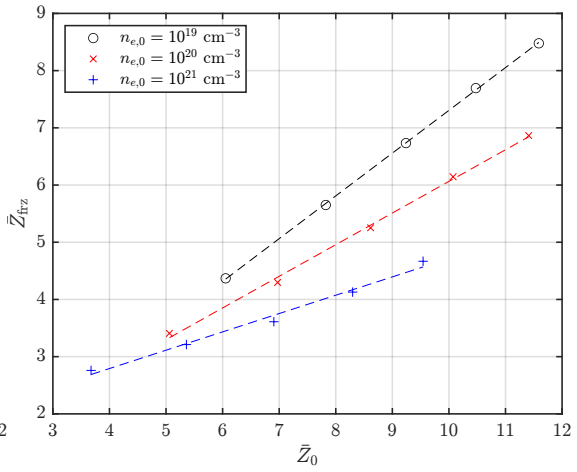

Figure 4.7: Freezing average charge against initial average charge, only TBR (according to Eq. (3.5)).

In Fig. 4.6, the freezing $\bar{Z}$ is plotted against the initial $\bar{Z}$ only considering the DR mechanism to study its effect on the ionization balance in isolation. First off, let us focus on the high-density case (blue) which remains near-constant at a value of $\bar{Z} = 3$. Since the included charge states only go as low as $\bar{Z} = 3$, we assume that either freezing has not set in before full recombination, or occurs at a value just above $\bar{Z} = 0$. This is likely due to the high initial density which allows for a large number of recombination events to occur, see also Eq. (4.1). By the time (in the expansion) the density has dropped to values too small to maintain considerable recombination, enough of it has already occurred. This prevents the freezing effect from setting in. Interestingly, for the initial densities of 10^{19} and 10^{20} cm^{-3}, freezing does set in. This is clearly seen in Figs. 4.8-4.9, where we show the temporal evolution of $\bar{Z}$ for two cases corresponding to two points from Fig. 4.6. The average charge stabilizes at a value larger than $\bar{Z} = 3$ which implies that the density and temperature after some time in the expansion does not yield significant recombination anymore. This takes around 20 ns case in Fig. 4.8 and only 3 ns for the case in Fig. 4.9, respectively corresponding to freezing distances of $r_{\mathrm{frz}} = 75$ mm and $r_{\mathrm{frz}} = 5$ mm following Eq. (4.6). We like to stress here that this occurs by taking into account *only* the DR mechanism. This is an interesting result, as the freezing effect is previously assumed to be intrinsically connected to the TBR mechanism (Sec. 3.3).

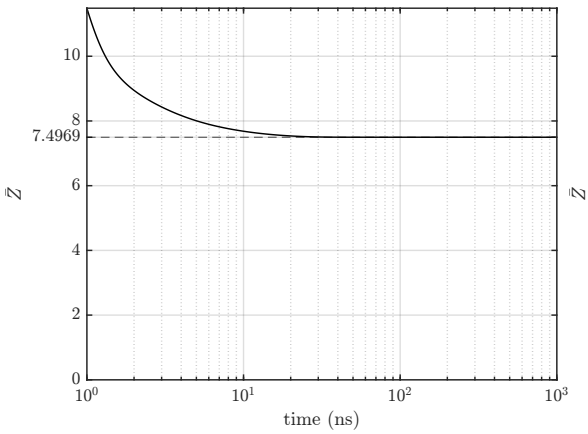

Figure 4.8: Average charge against time for $n_{e0} = 10^{19}$ cm^{-3}, $T_{e0} = 25$ eV.

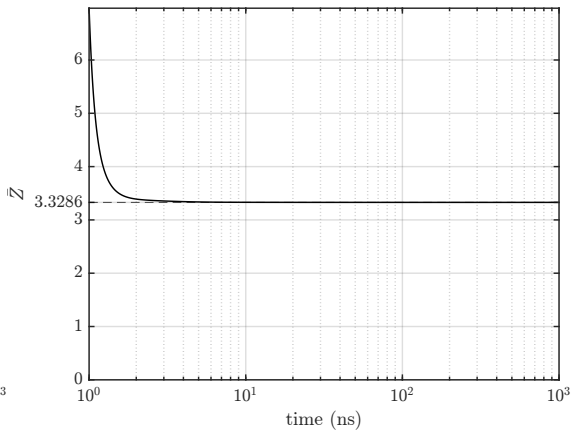

Figure 4.9: Average charge against time for $n_{e0} = 10^{20}$ cm^{-3}, $T_{e0} = 30$ eV.

In Fig. 4.7, we isolate the effect of the TBR mechanism, again by using Eq. (3.5). In essence, we consider here the theory on charge state freezing as presented in the current literature. The simulation results are very different from the DR case. First off, the freezing effect is present for all three densities. Secondly, by increasing the initial density the slope of the $\bar{Z}_{\text{frz}}$ vs. $\bar{Z}_0$ graphs decreases. It is clear, using this specific TBR rate, that freezing occurs for (almost) all sets of initial density and temperature included in the simulation. Moreover, the freezing charge is proportional to the initial charge for all temperatures included. We can take a closer look at the freezing characteristics using Fig. 4.10, where $\bar{Z}$ has been plotted against time for an initial temperature $T_{e0} = 20$ eV and three different densities. Again each case matches to an individual point depicted in Fig. 4.7. By keeping the initial temperature constant, we can further establish the density-dependence of the charge state freezing. This has most likely to do with the fact that lower-density trajectories in $\{T_e, n_e\}$-space require more time to reach the region where strong recombination takes place [26]. This explain the steeper drop in charge state for higher initial densities.

Most notable, however, is that the average charge stabilizes over a significantly longer timescale (tens μs) compared to the cases in Figs. 4.8 and 4.9 (tens of ns), where the DR mechanism is accounted for. As a result, the associated freezing distance also differs in over 2-3 orders of magnitude: by only considering TBR, one estimates the freezing distance to be ~ 1 meter. This is in line with literature on the topic, see Refs. [26, 27, 30]. Nevertheless, when DR is accounted for using Ref. [49], the distance is reduced to be on the scale of several mm's. As mentioned before, the length scale of the freezing effect is of great importance to validate the assumption of LTE ionization in e.g. RALEF-2D simulations.

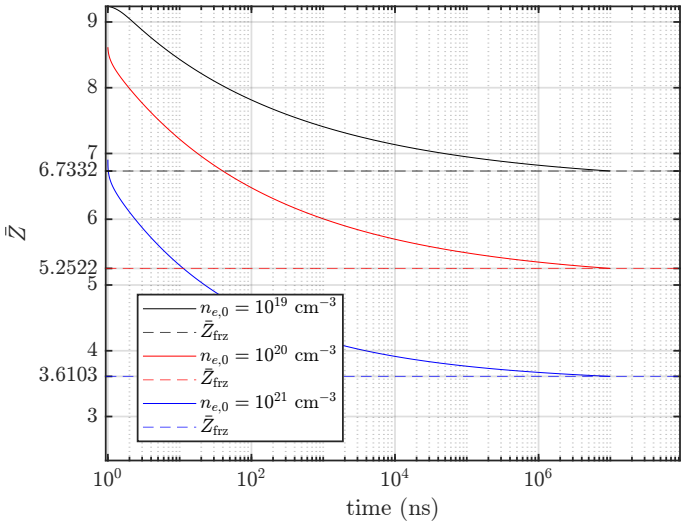

Figure 4.10: Average charge against time for $T_{e,0} = 20$ eV and $n_{e,0} = 10^{19}$ (black), $n_{e,0} = 10^{20}$ (red) and $n_{e,0} = 10^{21}$ (blue).

Next, we will look at two cases where both DR and TBR are included in the model. In Fig. 4.11, we reintroduce the TBR mechanism using the expression in Eq. (3.4) from Colombant *et. al.* [42]. We observe that this specific combination of the DR and TBR shows very similar results to the simulation outcomes with only DR in Fig. 4.6. For high densities (blue), the freezing effect is again not occurring. However, the same is now also the case for the moderate density simulations (red). By including the TBR mechanism on top of the DR, we essentially allow for more recombination to occur such that ions drop faster in charge state. This is also evident by looking at the low-density case (black), where the addition of TBR has shifted down the graph by approximately 1 compared to Fig. 4.6.

In Fig. 4.12, we again study the combination of the DR and TBR on the ionization balance but now using Eq. (3.5) from Roudskoy [29] for the TBR mechanism instead. Since we are using this specific rate, we also take into account the energy returning to the plasma by the X_{3b} term in Eq. (4.3). Although the overall simulation results look qualitatively similar to the previous cases, in the low-density case the charge states freeze out at overall higher values. This implies that the TBR mechanism has a greater effect on the ionization balance when Eq. (3.5) is used instead of Eq. (3.4). This is unsurprising as the Roudskoy rate contains a significantly stronger inverse scaling with T_e. In a decreasing temperature profile, the effect TBR hence starts to become more pronounced. In general, we have demonstrated that DR has a substantial effect on the ionization balance of expanding tin LPP and shows different freezing characteristics compared to the present literature which only treats the TBR mechanism. Even when we allow for DR and TBR to occur, the DR mechanism dominates the dynamics.

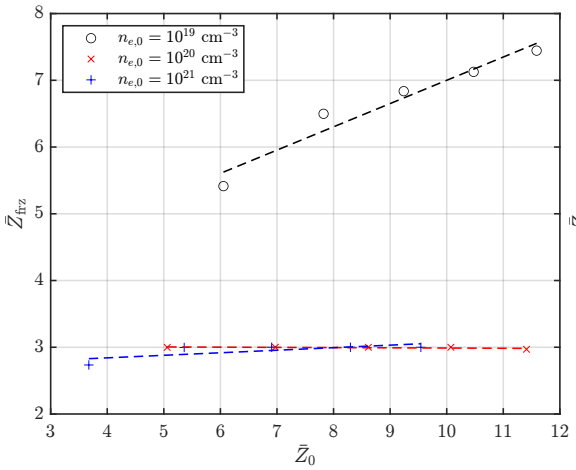

Figure 4.11: Freezing average charge against initial average charge for DR + TBR (according to Eq. (3.5)).

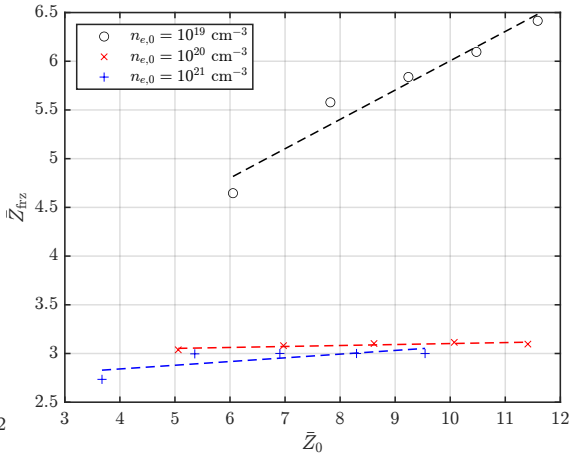

Figure 4.12: Freezing average charge against initial average charge for DR + TBR (according to Eq. (3.4)).

Note that we have left out radiative recombination from the model and hence assume its effect is negligibly small compared to DR and TBR. This is supported mainly by Figs. 3.5 and 3.6.

4.4 Connection to ion velocity and $\bar{Z}(E)$ invariance

Until now, this report covers two seemingly separate questions. First, in Ch. 1 and 2, we have taken notice of the (surprising) fact that the charge state detected some distance away from the target exhibits a consistent power-law dependence on the ion kinetic energy. Then, in Ch, 3 and 4, we went on to study the effect of recombination and charge state freezing using a numerical ion expansion model. This section is devoted to connecting the two lines of thought.

As the recombination rate is strongly dependent on the density, temperature and the charge state of the plasma, recombination proceeds at different rates in different sections of the expanding plasma. Although the current model misses the spatial dependence to separate out different plasma sections, we can assume a simplified model of the plasma at $t = t_0$. After the MP has irradiated the tin droplet, we can assume that the plasma generated is spherically symmetric with a diameter approximately equal to the laser diameter d_l. In this case, we can assume two gradients to be present. The first is a density gradient ∇n_e pointing to the target surface; the density near the surface is higher than some distance away from the surface. Second, an ion speed gradient ∇v_i points away from the target surface; ions located further away from the surface are given more

time to reach higher speeds. This is schematically depicted in Fig. 4.13. Consequently, fast ions find themselves in low-density regions and slow ions in high-density regions.

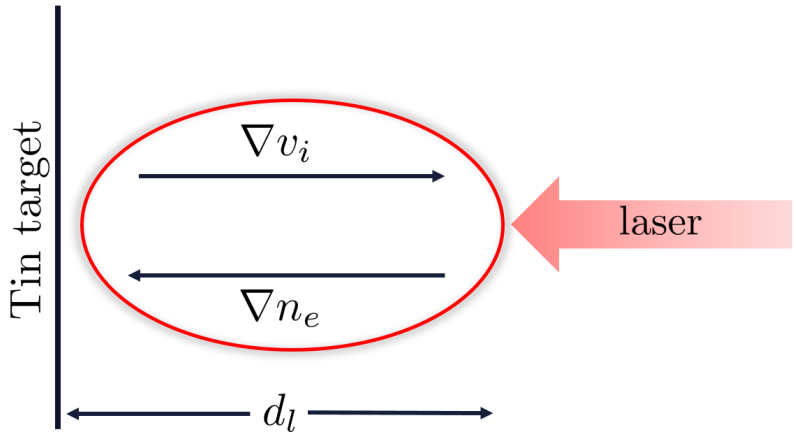

Figure 4.13: Schematic of the density and velocity gradient from the target. Adapted from Ref. [54].

Now, we bring in the considerations of the recombination study. If we consider Figs. 4.6-4.7 and 4.11-4.12, we can conclude that more overall recombination occurs at higher densities (this density-dependence has been covered in the previous section). This holds true for all cases; for both expressions of the TBR rate as well as the novel addition of DR. Since the slow-moving ions are located in the high-density regions, these will be subject to significantly more recombination compared to the fast-moving ions in the low-density regions further away from the target. In other words, *ions moving at higher speeds are able to retain a higher charge state.* This is in line with the experimental measurements introduced in Chapter 2, more specifically in Fig. 2.2 where we observe a shift of the ion energy spectrum peak for higher charge states and from the general shape of the $\bar{Z}(E)$-graph in Fig. 2.4.

Although we are able to recover the general $Z(E)$-trend from experiment, unfortunately this reasoning is not sufficient to explain the invariance of the specific power-law behaviour $\bar{Z} \propto E^{0.375}$. Nevertheless, some findings of the numerical model can may still be used to gain more insight. For example, it is evident for all cases presented in Figs. 4.6-4.7 and 4.11-4.12 that a proportionality between the average freezing charge and the initial charge exists. In other words, the functional relation between $\bar{Z}_{\text{frz}}$ and $\bar{Z}_0$ is found to be

$$\bar{Z}_{\text{frz}} \propto \varepsilon(n_e)\bar{Z}_0, \tag{4.7}$$

where $\varepsilon(n_e)$ is a density-dependent proportionality constant. Depending on which recombination mechanisms are taken into account and which analytical expressions are being used in the model, the slope changes. This proportionality may allow us to validate the use the theoretical arguments presented in Sec. 2.1.2, which were given for Z instead of $\bar{Z}_{\text{frz}}$.

5 Discussion and outlook

The work in this report directly motivates topics of further study. In this Chapter, we discuss the limitations of the results, and provide recommendations for the continuation of this work.

We start by highlighting some deficiencies of the time-dependent model presented in Chapter 4. First, the model assumes a homogeneous plasma that expands spherically at all times. This implies that more complex temperature and density profiles, also present in experiment, cannot be represented by the current model. Different components of the plasma are not spatially separated such that all electrons can recombine with all ions at each point in the simulation. As a result, the final average charge state may be underestimated compared to an experiment. For this reason, a logical extension of the time-dependent model would be to include the spatial expansion driven by plasma pressure gradients. This can be done by either coupling the results of the time-dependent to RALEF-2D, which can perform the full hydrodynamic calculation (both during and after the laser pulse is turned on). Alternatively, the rate equation solver can be coupled to a simpler hydrodynamic solver (see for example Refs. [29, 54]) which can track different plasma elements moving at different speeds after plasma formation.

Nevertheless, the current model is able to provide a solid understanding of how initial plasma conditions can affect the rates of different recombination mechanisms and ion properties throughout the expansion. Although highly idealized, the expansion *was* explicitly accounted for by assuming temporal profiles of the temperature and density. The time-dependent model was also improved in two ways compared to previous work [30]. First, the initial conditions for the fractional ion population used in simulation were significantly more accurate by making use of the ATOMIC code. Secondly, the rates of the DR mechanism are implemented using comprehensive atomic calculations from Ref. [49], opposed to much simpler approximation laws. In light of the lack of consensus, future work should look into ways to replace the approximation laws for TBR in a similar way. These can be easily implemented using the code presented in this work.

One of the more interesting findings from this work is the importance of the DR mechanism for tin in the expansion phase, which has not been documented in literature as of yet. This argument is reinforced by the fact that we used the most detailed atomic calculations for the DR rates to date instead of approximation laws. However, to further investigate how the effect of DR quantitatively compares to the effect of TBR, the approximation laws of TBR ought be replaced as well. Anyway, the role of DR in the context of expanding plasmas deserves further study, for example by (i) extending the electron temperature and density range, (ii) extrapolating to more charge states ($Z \leq< 3$ and $Z > 13$) in simulation and (iii) considering other atomic species. This latter point is interesting because the importance of the DR process to the ionization balance has already been established in other species [55, 56], but not in the context of expansion. By broadening the research scope, the applicability of this type of atomic calculations on the DR process in this context (expansion of hot and dense heavy-species plasmas) should be further established.

It is evident that most aspects of this work would benefit from a more rigorous treatment of the hydrodynamic processes in the expansion. The role of DR in such a model would be, in light

of the results presented here, an extremely interesting topic of further study. It would also allow for a *direct* comparison to the measured ion energy spectrum and the $\bar{Z}(E)$ invariance. Although the time-dependent model has provided qualitative arguments for the ion energy spectra (see Sec. 4.4), it will require the hydrodynamic treatment (similar to e.g. Ref. [29]) to further elucidate the specific ion energy spectra and invariance of the average charge state. Nevertheless, we have demonstrated both the importance of accounting for recombination process in plasmas relevant to EUV lithography machines, and have taken first steps towards accurately modelling them. The more detailed characterization of expanding tin plasmas is imperative to the design of effective ion mitigation schemes in future lithography machines.

6 Conclusion

This report focused on the role of recombination processes in an expanding laser-produced tin plasma relevant to EUV lithography, in particular the temporal evolution of charge-state populations. The main findings of this work can be summarized as follows:

- **Based on atomic calculations, dielectronic recombination is of great importance in determining the ionization balance of an expanding tin LPP.**
- **Freezing of charge states is not solely dependent on the three-body recombination mechanism.**
- **The length scale associated with the freezing effect, which determines the extent to which the LTE ionization assumption in RALEF-2D is valid, is reduced by several orders of magnitudes when taking DR into account.**
- **Faster ions retain higher charge states by considering the density-dependence of (all) recombination mechanisms.**

Bibliography

[1] Gerd Schneider, Peter Guttmann, Stefan Heim, Stefan Rehbein, Florian Mueller, Kunio Nagashima, J Bernard Heymann, Waltraud G Müller, and James G McNally. Three-dimensional cellular ultrastructure resolved by x-ray microscopy. *Nature methods*, 7(12):985–987, 2010. 1

[2] T Helk, Michael Zürch, and C Spielmann. Perspective: Towards single shot time-resolved microscopy using short wavelength table-top light sources. *Structural Dynamics*, 6(1):010902, 2019. 1

[3] Anne Sakdinawat and David Attwood. Nanoscale x-ray imaging. *Nature photonics*, 4(12):840–848, 2010. 1

[4] A Bartnik, H Fiedorowicz, R Jarocki, J Kostecki, M Szczurek, and PW Wachulak. Laser-plasma euv source dedicated for surface processing of polymers. *Nuclear Instruments and Methods in Physics Research Section A: Accelerators, Spectrometers, Detectors and Associated Equipment*, 647(1):125–131, 2011. 1

[5] Davide Bleiner, John Costello, Francois de Dortan, Gerry O'Sullivan, Ladislav Pina, and Alan Michette. *Short Wavelength Laboratory Sources: Principles and Practices*. Royal Society of Chemistry, 2014. 1

[6] Gordon E Moore et al. Cramming more components onto integrated circuits, 1965. 1

[7] Jan van Schoot, Kars Troost, Frank Bornebroek, Rob van Ballegoij, Sjoerd Lok, Peter Krabbendam, Judon Stoeldraijer, Jos Benschop, Jo Finders, Hans Meiling, et al. The future of euv lithography: continuing moore's law into the next decade. In *Extreme Ultraviolet (EUV) Lithography IX*, volume 10583, page 105830R. SPIE, 2018. 1

[8] V Bakshi. Euv lithography 2nd edn (bellingham, wa, 2018. 1, 2

[9] Igor Fomenkov, David Brandt, Alex Ershov, Alexander Schafgans, Yezheng Tao, Georgiy Vaschenko, Slava Rokitski, Michael Kats, Michael Vargas, Michael Purvis, Rob Rafac, Bruno La Fontaine, Silvia De Dea, Andrew LaForge, Jayson Stewart, Steven Chang, Matthew Graham, Daniel Riggs, Ted Taylor, Mathew Abraham, and Daniel Brown. Light sources for high-volume manufacturing euv lithography: technology, performance, and power scaling. *Advanced Optical Technologies*, 6(3-4):173–186, 2017. 1

[10] DC Brandt, I Fomenkov, and J Stewart. Extreme ultraviolet (euv) lithography xi, 2020. 1

[11] Oscar O Versolato. Physics of laser-driven tin plasma sources of euv radiation for nanolithography. *Plasma Sources Science and Technology*, 28(8):083001, 2019. 1, 18

[12] Hanneke Gelderblom, Henri Lhuissier, Alexander L Klein, Wilco Bouwhuis, Detlef Lohse, Emmanuel Villermaux, and Jacco H Snoeijer. Drop deformation by laser-pulse impact. *Journal of fluid mechanics*, 794:676–699, 2016. 2

[13] Dmitry Kurilovich, Alexander L Klein, Francesco Torretti, Adam Lassise, Ronnie Hoekstra, Wim Ubachs, Hanneke Gelderblom, and Oscar O Versolato. Plasma propulsion of a metallic microdroplet and its deformation upon laser impact. *Physical review applied*, 6(1):014018, 2016. 2

[14] Bo Liu. Morphology of liquid tin sheets formed by laser impact on droplets. 2022. 2

[15] R. Schupp, F. Torretti, R.A. Meijer, M. Bayraktar, J. Scheers, D. Kurilovich, A. Bayerle, K.S.E. Eikema, S. Witte, W. Ubachs, R. Hoekstra, and O.O. Versolato. Efficient generation of extreme ultraviolet light from Nd:yag-driven microdroplet-tin plasma. *Phys. Rev. Appl.*, 12:014010, Jul 2019. 2

[16] Lars Behnke, Ruben Schupp, Zoi Bouza, Muharrem Bayraktar, Zeudi Mazzotta, R Meijer, J Sheil, S Witte, W Ubachs, Ronnie Hoekstra, et al. Extreme ultraviolet light from a tin plasma driven by a 2-μm-wavelength laser. *Optics express*, 29(3):4475–4487, 2021. 2

[17] Gerry O'Sullivan, Bowen Li, Rebekah D'Arcy, Padraig Dunne, Paddy Hayden, Deirdre Kilbane, Tom McCormack, Hayato Ohashi, Fergal O'Reilly, Paul Sheridan, et al. Spectroscopy of highly charged ions and its relevance to euv and soft x-ray source development. *Journal of Physics B: Atomic, Molecular and Optical Physics*, 48(14):144025, 2015. 2

[18] Sasa Bajt, Jennifer B Alameda, Troy W Barbee Jr, W Miles Clift, James A Folta, Benjamin B Kaufmann, and Eberhard Adolf Spiller. Improved reflectance and stability of mo/si multilayers. *Optical engineering*, 41(8):1797–1804, 2002. 2

[19] John Sheil, Oscar O Versolato, Amanda J Neukirch, and J Colgan. Multiply-excited states and their contribution to opacity in co2 laser-driven tin-plasma conditions. *Journal of Physics B: Atomic, Molecular and Optical Physics*, 54(3):035002, 2021. 2, 18

[20] Francesco Torretti, John Sheil, Ruben Schupp, MM Basko, Muharrem Bayraktar, RA Meijer, Stefan Witte, Wim Ubachs, Ronnie Hoekstra, OO Versolato, et al. Prominent radiative contributions from multiply-excited states in laser-produced tin plasma for nanolithography. *Nature communications*, 11(1):1–8, 2020. 2, 18

[21] V Ye Banine, KN Koshelev, and GHPM Swinkels. Physical processes in euv sources for microlithography. *Journal of Physics D: Applied Physics*, 44(25):253001, 2011. 2

[22] Daisuke Nakamura, Koji Tamaru, Yuki Hashimoto, Tatsuo Okada, Hiroki Tanaka, and Akihiko Takahashi. Mitigation of fast ions generated from laser-produced sn plasma for extreme ultraviolet light source by h 2 gas. *Journal of Applied Physics*, 102(12):123310, 2007. 2

[23] DB Abramenko, MV Spiridonov, PV Krainov, VM Krivtsun, DI Astakhov, VV Medvedev, M van Kampen, D Smeets, and KN Koshelev. Measurements of hydrogen gas stopping efficiency for tin ions from laser-produced plasma. *Applied Physics Letters*, 112(16):164102, 2018. 2

[24] SS Harilal, Beau O'Shay, and Mark S Tillack. Debris mitigation in a laser-produced tin plume using a magnetic field, 2005. 2

[25] Yoshifumi Ueno, Georg Soumagne, Akira Sumitani, Akira Endo, Takeshi Higashiguchi, and Noboru Yugami. Reduction of debris of a co 2 laser-produced sn plasma extreme ultraviolet source using a magnetic field. *Applied Physics Letters*, 92(21):211503, 2008. 2

[26] RR Goforth and P Hammerling. Recombination in an expanding laser-produced plasma. *Journal of Applied Physics*, 47(9):3918–3922, 1976. 3, 11, 14, 15, 17, 22

[27] GJ Tallents. An experimental study of recombination in a laser-produced plasma. *Plasma Physics*, 22(7):709, 1980. 3, 11, 14, 15, 22

[28] PD Gupta, PA Naik, and HC Pant. Effect of recombination on ion expansion velocity in laser-produced plasmas. *Journal of applied physics*, 55(3):701–703, 1984. 3

[29] IV Roudskoy. General features of highly charged ion generation in laser-produced plasmas. *Laser and Particle beams*, 14(3):369–384, 1996. 3, 14, 15, 23, 25, 26

[30] Russell A. Burdt, Yezheng Tao, Mark S. Tillack, Sam Yuspeh, Nek M. Shaikh, Eli Flaxer, and Farrokh Najmabadi. Laser wavelength effects on the charge state resolved ion energy distributions from laser-produced sn plasma. *Journal of Applied Physics*, 107(4):043303, 2010. 3, 11, 14, 15, 17, 22, 25

[31] Mikhail Basko and J. Maruhn. Development of a 2d radiation-hydrodynamics code ralef for laser plasma simulations. 01 2010. 4

[32] L Poirier, A Lassise, Y Mostafa, L Behnke, N Braaksma, L Assink, R Hoekstra, and OO Versolato. Energy-and charge-state-resolved spectrometry of tin laser-produced plasma using a retarding field energy analyzer. *Applied Physics B*, 128(7):1–7, 2022. 4, 5

[33] L Poirier, A Bayerle, A Lassise, F Torretti, R Schupp, L Behnke, Y Mostafa, W Ubachs, OO Versolato, and R Hoekstra. Cross-calibration of a combined electrostatic and time-of-flight analyzer for energy-and charge-state-resolved spectrometry of tin laser-produced plasma. *Applied Physics B*, 128(3):1–11, 2022. 4

[34] Lucas Poirier, Diko J Hemminga, Adam Lassise, Luc Assink, Ronnie Hoekstra, John Sheil, and Oscar O Versolato. Strongly anisotropic ion emission in the expansion of nd: Yag-laser-produced plasma. *Physics of Plasmas*, 29(12):123102, 2022. 4, 9

[35] Markus Brandstätter, Marco M Weber, and Reza S Abhari. Non-axisymmetric droplet irradiation effects on ion and extreme ultraviolet light emission of laser-produced plasma light sources. *Journal of Applied Physics*, 129(23):233306, 2021. 4

[36] Russell A Burdt, Sam Yuspeh, Kevin L Sequoia, Yezheng Tao, Mark S Tillack, and Farrokh Najmabadi. Experimental scaling law for mass ablation rate from a sn plasma generated by a 1064 nm laser. *Journal of Applied Physics*, 106(3):033310, 2009. 4, 14

[37] DJ Hemminga, L Poirier, MM Basko, R Hoekstra, W Ubachs, OO Versolato, and J Sheil. High-energy ions from nd: Yag laser ablation of tin microdroplets: comparison between experiment and a single-fluid hydrodynamic model. *Plasma Sources Science and Technology*, 30(10):105006, 2021. 5, 8, 9

[38] Patrick Mora. Plasma expansion into a vacuum. *Physical Review Letters*, 90(18):185002, 2003. 8, 9

[39] M Murakami, Y-G Kang, K Nishihara, S Fujioka, and H Nishimura. Ion energy spectrum of expanding laser-plasma with limited mass. *Physics of plasmas*, 12(6):062706, 2005. 8, 9

[40] MM Basko, VG Novikov, and AS Grushin. On the structure of quasi-stationary laser ablation fronts in strongly radiating plasmas. *Physics of Plasmas*, 22(5):053111, 2015. 8

[41] DJ Hemminga, OO Versolato, and J Sheil. Characterization of plasmas driven by laser wavelengths in the 1.064-10.6\mu m range as future extreme ultraviolet light sources. *arXiv preprint arXiv:2208.14223*, 2022. 8

[42] D Colombant and GF Tonon. X-ray emission in laser-produced plasmas. *Journal of Applied Physics*, 44(8):3524–3537, 1973. 11, 14, 16, 17, 22

[43] RWP McWhirter. Plasma diagnostic techniques. edited by richard h. huddlestone and stanley l. leonard. library of congress catalog card number 65-22763, 1965. 11

[44] MJ Seaton. The solution of capture–cascade equations for hydrogen. *Monthly Notices of the Royal Astronomical Society*, 119(2):90–97, 1959. 11

[45] Alan C Kolb and RWP McWhirter. Ionization rates and power loss from θ-pinches by impurity radiation. *The Physics of fluids*, 7(4):519–531, 1964. 11

[46] NJ Peacock and RS Pease. Sources of highly stripped ions. *Journal of Physics D: Applied Physics*, 2(12):1705, 1969. 11

[47] IV Roudskoy. General features of highly charged ion generation in laser-produced plasmas. *Laser and Particle beams*, 14(3):369–384, 1996. 11, 14

[48] AV Gurevich and LP Pitaevskii. Recombination coefficient in a dense low-temperature plasma. *Sov. Phys. JETP*, 19(4):870, 1964. 11, 12

[49] NR Badnell, A Foster, DC Griffin, D Kilbane, M O'Mullane, and HP Summers. Dielectronic recombination of heavy species: the tin 4p64dq- 4p64d (q- 1) 4f+ 4p54d (q+ 1) transition arrays for q= 1–10. *Journal of Physics B: Atomic, Molecular and Optical Physics*, 44(13):135201, 2011. 12, 13, 14, 15, 22, 25

[50] Ya B Zel'Dovich and Yu P Raizer. *Physics of shock waves and high-temperature hydrodynamic phenomena*. Courier Corporation, 2002. 17

[51] Y Tao, MS Tillack, S Yuseph, R Burdt, and F Najmabadi. Nonclassical hydrodynamic behavior of sn plasma irradiated with a long duration co2 laser pulse. *Applied Physics B*, 99(3):397–400, 2010. 17

[52] P Hakel, ME Sherrill, S Mazevet, J Abdallah Jr, J Colgan, DP Kilcrease, NH Magee, CJ Fontes, and HL Zhang. The new los alamos opacity code atomic. *Journal of Quantitative Spectroscopy and Radiative Transfer*, 99(1-3):265–271, 2006. 18

[53] DP Kilcrease, J Colgan, P Hakel, CJ Fontes, and ME Sherrill. An equation of state for partially ionized plasmas: The coulomb contribution to the free energy. *High Energy Density Physics*, 16:36–40, 2015. 18

[54] Russell Allen Burdt. *Ion emission and expansion in laser-produced tin plasma*. University of California, San Diego, 2011. 24, 25

[55] LU Haidong, SU Maogen, MIN Qi, CAO Shiquan, HE Siqi, DONG Chenzhong, and FU Yanbiao. Effect of dielectronic recombination on charge-state distribution in laser-produced plasma based on steady-state collisional-radiative models. *Plasma Science and Technology*, 22(10):105001, 2020. 25

[56] BW Li, Gerry O'Sullivan, YB Fu, and CZ Dong. Dielectronic recombination of pd-like gadolinium. *Physical Review A*, 85(1):012712, 2012. 25